The Toughness of High-Strength Steel Weld Metals

High weld toughness can be achieved by using an inert shielding gas during welding to reduce oxide inclusions in the weld metal

BY T. DAI, Z. FENG, D. KYLE, S. A. DAVID, K. M. SEBECK, D. A. TZELEPIS, K. VIEAU, AND M. ROGERS

Abstract

Low-temperature phase transformation (LTPT) welding consumables are a new class of welding wires developed to mitigate hydrogen-induced cracking in the welding of high-strength steels without preheating or postweld heat treatment. LTPT weld metals have a high strength, but their toughness needs further investigation. LTPT weld metals predominately contain a martensite microstructure, which is necessary to achieve high strength; however, martensitic weld metals containing oxide inclusions have relatively poor toughness. Three welding processes — gas metal arc welding (GMAW), gas tungsten arc welding (GTAW), and hot wire GTAW — were investigated. Optical microscopy, scanning electron microscopes, and transmission electron microscopes were employed for characterization. The role of the shielding gas in the formation of oxide inclusions in LTPT weld metals was investigated. The formation of oxide inclusions in the weld metals was related to the CO_2 in the shielding gas. When 100% Ar or a pure inert shielding gas mixture was used for all three welding processes, oxide inclusions were greatly reduced, and the weld metal toughness improved considerably, matching the base metal toughness. The mechanism by which inclusions promote fracture propagation in the weld metal was proposed.

Keywords

- Low-Temperature Phase Transformation (LTPT)
- Weld Consumable
- High-Strength Steels
- Arc Welding
- Impact Toughness
- Inclusions

Introduction

The toughness of steels and their weld metals is among their most important property for critical structural applications. Modern high-strength steels are generally designed for excellent strength and toughness. For example, American Petroleum Institute (API) Specification 5L, *Specification for Line Pipe*, has a much higher Charpy V-notch absorbed energy requirement for X100 steel than for X60 steel of product standard level (PSL) 2 pipe grade (Ref. 1). Weld metal strength and toughness are highly dependent on the weld microstructure. For low-alloy steels with strength levels up to 101–116 ksi (700–800 MPa), acicular ferrite is considered to be the most desirable microstructure for achieving a good combination of strength and toughness (Refs. 2, 3); several investigations have revealed the acicular ferrite microstructure and its relationship to toughness (Refs. 4–9). Acicular ferrite is the most common microstructure observed in weld metals for low-alloy steels (Refs. 10, 11).

For even higher-strength alloy steels, such as those with strengths of more than 145 ksi (1000 MPa), the acicular ferrite microstructure alone is often inadequate to achieve the required degree of strength. For example, as-welded 12.5Cr-5Ni weld metal has a martensitic microstructure with high toughness (Ref. 12). Norstrom et al. found that, in martensitic weld metals, the

https://10.29391/2022.101.006

Fig. 1 — A — Example of the weld plates (T17, 46100/1766, GTAW-HW) with the layout for cutting the Charpy impact samples and a metallography sample; B — example of the X65 pipeline weld coupon (X65/1764, GTAW-HW).

martensite packet size in quenched and moderately tempered low-carbon lath martensite could control toughness (Ref. 13). Cao et al. reported that the size of bainite packets with high-angle grain boundaries (>15 deg) influenced the toughness as well (Ref. 14).

Qiu et al. (Ref. 15) found that when a filler wire of the composition 0.049 C-0.61 Si-0.71 Mn-17.7 Cr-7.13 Ni-73.8 Fe (wt-%) was diluted with the base metal, the weld metal microstructure contained martensite and retained austenite. Weld metals used during gas metal arc welding (GMAW) with 100% CO_2 shielding gas have low toughness at 313 and 273 K, with an absorbed energy of only 15–40 J (Ref. 15). Fully martensitic weld metal has the lowest toughness (15–20 J) (Ref. 15). In the work of Keehan et al. (Refs. 16, 17), a metal used for shielded metal arc welding consisting of 0.031 C-0.27 Si-2.1 Mn-0.011 P-0.008S-0.48 Cr-9.2 Ni-0.64 Mo-87.26 Fe (wt-%) had a martensitic/bainitic microstructure. The yield strength was found to be 848 MPa (123 ksi), and the ultimate tensile strength was 1051 MPa (152.4 ksi). However, the toughness-absorbed energy at 20°C was only 16 J. Zhang et al. (Ref. 18) investigated three weld metals using GMAW and CO_2 shielding gas. The weld metal with the highest hardness and wear resistance contained martensite plus other reinforcing phases, but it had the lowest impact toughness compared with martensitic weld metals with few precipitates.

Barrick et al. (Ref. 19) investigated Ni10 martensitic welds produced using gas tungsten arc welding (GTAW) (100% Ar), GMAW (98% Ar, 2% O_2), and GMAW (100% Ar). They ranked GTAW (100% Ar) as having the highest toughness, GMAW (100% Ar) the second highest, and GMAW (98% Ar, 2% O_2) the lowest. GTAW (100% Ar) welds contained the fewest inclusions and thus had the highest toughness. GMAW (100% Ar) welds had a similar number of inclusions to GMAW (98% Ar, 2% O_2) welds, but the inclusion sizes in the former were smaller than in the latter. According Barrick et al., larger inclusion sizes resulted in lower toughness (Ref. 19). However, the nature of the inclusions in this study was not reported.

During welding, residual stresses contribute to the overall stress state of the weldment. These stresses are tensile in nature and contribute to stress corrosion cracking (SCC) and fatigue. A concept showing much promise for improving SCC and fatigue is the use of low-temperature phase transformation (LTPT) wires. They reduce the formation of tensile residual stresses in welded structures by exploiting the volume expansion during martensitic phase transformation to compensate for thermal contraction. In the 1970s, Jones and Alberry (Ref. 20) were among the first suggesting that tensile residual stresses are best avoided by reducing the M_s temperature so phase change can continue to compensate for the accumulation of tensile strains in the weld during cooling to room temperature. The LTPT welding wires typically have a chemistry of 0–15 wt-% Ni and 0–15 wt-% Cr for martensitic transformation at low temperatures.

In this work, we investigated the weld metal toughness of LTPT welding wires for use in high-strength and ultra-high-strength steels. Recently, Oak Ridge National Laboratory (ORNL), in cooperation with the U.S. Army and other partners, developed a class of LTPT welding wires that avoid hydrogen-induced cracking (HIC) in high-strength and ultra-high-strength steel welds. These steels typically have martensitic microstructures with high hardness that are prone to HIC (Refs. 21–24). Compressive residual stress is formed in the weld region as a result of the volumetric expansion of martensite through a very low-temperature martensitic phase transformation (Ref. 25).

The LTPT welding wire was formulated to have a martensitic phase transformation temperature much lower than the normal decomposition temperature range of the base metal. The LTPT welding wire has shown successful mitigation of HIC in welds of high-strength steels. Most notably, it eliminates the need for preheating and postweld heat treatment in pipeline steels, ultra-high-strength steels, and carbon-rich ultra-high-strength armor steels. ORNL's LTPT welding wire can produce a high-strength

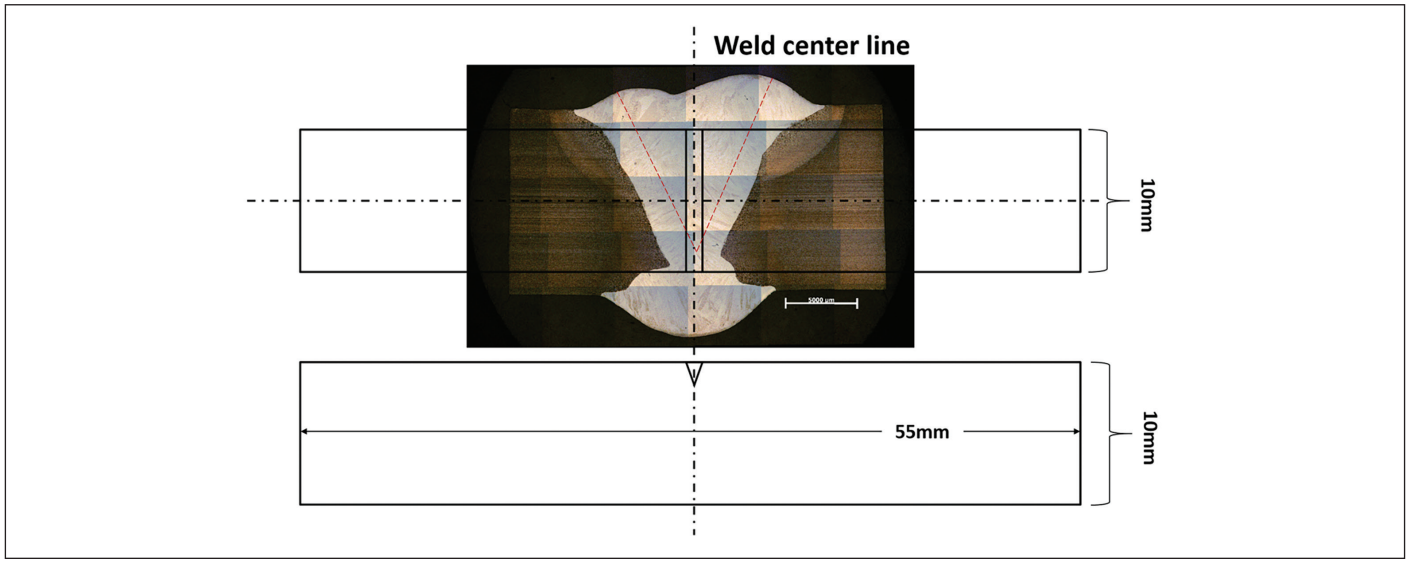

Fig. 2 — The cross-section overview of an armor steel weld and the position of the Charpy V-notch impact toughness test sample (highlighted with black lines) as well as the region for weld chemistry analysis (highlighted by the red dashed lines).

weld, typically overmatching the strength of high-strength steels such as armor and pipeline steels. Similar to welds made with other high-strength steel welding wires (Refs. 26, 27) using GMAW, the LTPT weld showed low toughness.

The present work investigated the effects of different welding processes and shielding gases on the toughness of LTPT welds. It also focused on determining the root causes of the low toughness of LTPT weld metals, leading to the development of welding conditions/techniques that improved weld toughness.

Materials and Experiments

Materials and Welding Parameters

The investigation was carried out on three types of high-strength steels: 1) two armor steels, MIL-DTL-46100 and MIL-DTL-12560, in the form of 0.5-in.-thick plates (Ref. 28); 2) X65 pipeline steel with an outside diameter of 8.625 in. and a wall thickness of 0.5 in.; and 3) a new class of armor steel — FeMnAl steel — in the form of 0.5-in.-thick plates. The typical composition of FeMnAl steel is Fe-30 Mn-9 Al-1 Si-0.9C-0.5 Mo (wt-%) (Ref. 29). Two LTPT filler wires developed at ORNL were used in this effort; they are designated as LTPT1764 and LTPT1766. Their chemical compositions are similar, and they are not commercially available.

Three welding processes — GMAW, GTAW, and hot wire GTAW (GTAW-HW) — were carried out with base metal/filler metal combinations as well as the corresponding welding processes and shielding gases. They are listed in Table 1. The joint design for the MIL-DTL-46100 and MIL-DTL-12560 plates and the new FeMnAl armor steel plates was a 30-deg single-V groove. The joint design for the X65 pipeline steel was a 37-deg single-V groove. The representative welding parameters for a typical armor steel weld T17 (46100/1766, GTAW-HW) are given in Table 2. Figure 1 shows the appearance of the welds made in this study, both using GTAW-HW: weld ID T17 on the 46100 plate with the LTPT 1766 wire and weld ID X65-3 on the X65 steel pipe with the LTPT 1764 wire.

Microstructure Characterization, Toughness Test, and Chemical Analysis

After welding, the metallographic specimens were prepared for optical microscopy using conventional metallography techniques. Each sample was chemically etched using 5% Nital (5 vol-% nitric acid and 95 vol-% ethyl alcohol), and its macrostructure was observed under a Zeiss Axio Imager.A2 microscope. The microhardnesses across the weld metals were measured using the Vickers hardness indenter LECO LM100AT with a 100-g load ($HV_{0.1}$). The samples were then repolished and swabbing-etched using an etchant with the composition of 20-mL glycerol, 30-mL HCl, 10-mL HNO_3 for characterization of the microstructure under the Zeiss microscope. Further characterization was carried out using a TESCAN MIRA3 scanning electron microscope (SEM), including electron backscatter diffraction analysis.

Charpy V-notch samples were machined for the impact toughness tests. All the samples were notched at the weld center line, as shown in Fig. 2. The toughness test samples were 10 × 10 × 55 mm, in accordance with ASTM E23, *Standard Test Methods for Notched Bar Impact Testing of Metallic Materials* (Ref. 30). The Charpy V-notch toughness tests were conducted using a Tinius Olsen model 84 pendulum impact tester. All the welds were tested at room temperature, 23 ± 2°C (~ 73°F); selected welds were also tested at 0°C (32°F) and −40°C (−40°F).

After the toughness test, the fracture surfaces were characterized and quantitatively analyzed using an SEM. Scanning transmission electron microscopy/energy-dispersive x-ray spectroscopy (STEM/EDX) was used to analyze the chemical composition of the inclusions on the fracture surfaces. STEM and EDX were performed using a ThermoFisher Scientific Talos F200X transmission electron microscope (TEM) STEM instrument

Table 1 — The Base Metals, Filler Metals, Welding Methods, and Shielding Gases Used in This Study

Weld	T1	T2	T3	T4	T5	T6	T7
Base metal/ filler metal	12560/1764	46100/1764	46100/1766	12560/1766	46100/1766	46100/1766	46100/1766
Welding method	GMAW	GMAW	GMAW	GMAW	GTAW	GMAW	GMAW
Shielding gas	95% Ar 5% CO_2	95% Ar 5% CO_2	95% Ar 5% CO_2	95% Ar 5% CO_2	100% Ar	75% Ar 25% He	98% Ar 2% H_2
Weld	**T14**	**T15**	**T16**	**T17**	**T18**	**T19**	**X65-1**
Base metal/ filler metal	46100/1766	46100/1766	46100/1766	46100/1766	46100/1764	12560/1764	X65/1764
Welding method	GMAW-P	GMAW	GMAW-P	GTAW-HW	GTAW-HW	GTAW-HW	GMAW
Shielding gas	99% Ar 1% CO_2	97% Ar 2% CO_2 1% H_2	63% Ar 35% He 2% CO_2	100% Ar	100% Ar	100% Ar	98% Ar 2% CO_2

operated at 200 keV. The sample for inclusion analysis using STEM EDX was prepared using a focused ion beam (FIB) system.

The weld metals of the 46100/1766, 12560/1766, X65/1764, and FeMnAl/1764 welds were extracted for chemical analysis according to CAP-017Q (inductively coupled plasma atomic emission spectroscopy [ICP-AES]) and ASTM E 1019-18, *Standard Test Methods For Determination of Carbon, Sulfur, Nitrogen, and Oxygen In Steel, Iron, Nickel, and Cobalt Alloys by Various Combustion and Inert Gas Fusion Techniques By Various Combustion And Inert Gas Fusion Techniques*. The samples were taken in the region within the red dashed lines, as shown in Fig. 2. They were tested for Al, C, Co, Cr, Cu, Fe, Mn, Mo, Ni, O, P, S, Se, Si, and Zn content. The carbon content was determined by combustion-infrared absorbance, and the oxygen content was determined by inert gas fusion.

Results

Macrostructure and Hardness Profiles

Figure 3 shows the macrostructures and hardness profiles of welds X65/1764, 12560/1764, 46100/1764, and FeMnAl/1764, all which were made with the GMAW process. The FeMnAl/1764 weld was a double-V-groove joint, and the other three were single-V-groove weld joints. All welds passed nondestructive examination conducted according to ASME *Boiler and Pressure Vessel Code*, Section IX, Radiographic Examination (QW-191.1). No weld defects were found.

As shown in Fig. 3, the four welds exhibited very different microhardness variations, but they represented the overall characteristics of the hardness variations in each type of weld made with different steel and welding wire combinations. Table 3 lists the characteristic hardness values of the different regions (base metal, weld metal, and heat-affected zone [HAZ]) of the welds of the four base metals (X65, 12560, 46100, and FeMnAl). The X65 base metal had the lowest hardness, 204 $HV_{0.1}$, and the armor steel 46100 base metal had the highest hardness, 608 $HV_{0.1}$. Due to the dilution between the welding wire and base metal, the weld metal hardnesses of the four welds were very different even though the same filler wire, LTPT1764, was used. The hardness of the LTPT1764 welding wire was 347 $HV_{0.1}$. The weld metal hardness of FeMnAl was 183 $HV_{0.1}$, the lowest among all the weld metals, whereas the hardness of the other three welds were in the range of 370–450 $HV_{0.1}$. The low hardness in the FeMnAl/1764 weld metal suggests that, due to the high-level of Mn and Al in the FeMnAl base metal, the weld metal remained austenite during cooling — Fig. 3F.

As shown Fig. 3 and Table 3, the microhardness in the HAZ of the four welds was also quite different. The X65 showed a gradual increase in microhardness in the HAZ, reaching the peak value of 250 HV near the weld interface. Both 12560 and 46100 armor steel, having a higher hardenability and a high carbon level, had a much-hardened HAZ near the weld interface. But they also had a considerable reduction in the microhardness in the far HAZ approximately 3–4 mm away from the weld interface. Such HAZ softening is typical in the armor steel and other high-strength steels as a result of over-tempering of the martensite and other hardened phases in the base metal. The HAZ of the FeMnAl steel

T8	T9	T12	T13
46100/1766	46100/1766	12560/1766	46100/1766
GMAW	GMAW	GTAW-HW	GTAW-HW
98% Ar 2% CO_2	90% Ar 8% He 2% CO_2	100% Ar	100% Ar
X65-2	**X65-3**	**FeMnAl-1**	**FeMnAl-2**
X65/1766	X65/1764	FeMnAl/ 1764	FeMnAl/ 1764
GMAW	GTAW-HW	GMAW	GTAW
98% Ar 2% CO_2	100% Ar	75% Ar 25% He	75% Ar 25% He

weld was quite different, characterized by a wide and softened HAZ.

The hardness profile of the 46100/1766 single-V-groove weld was similar to the hardness profile of the 46100/1764 weld, as shown in Fig. 3C. The highest hardness was in the HAZ, and the lowest hardness point was in the over-tempered zone. In Table 4, the 46100/1766 weld metal hardness was ~ 410–450 $HV_{0.1}$, lower than the HAZ hardness, which was ~ 580–600 $HV_{0.1}$. Neither the shielding gas nor the welding method (GMAW, GTAW, and GTAW-HW) had an obvious influence on the weld metal hardness. The lowest hardness point was a narrow over-tempered region just outside the fine-grain HAZ. The over-tempered region hardness was 330–350 $HV_{0.1}$ for all the 46100/1766 welds.

Microstructure Characterization

Under optical microscopy, the martensitic lath structure was evident in the weld metal for the armor steel joints. Three typical examples of the microstructure under optical microscopy are shown in Fig. 4A, C, and E. In Fig. 4C, the lath structure is observed under the relief of the dendrite structure. There are many black dots in Fig. 4A. Under SEM, the black dots appeared to be small holes, as shown in Fig. 4B. They were the original positions of the inclusions. In Fig. 4F, an inclusion can be found on the surface at its hole (position). The number of holes indicated that the weld metal using shielding gas with a higher CO_2 content contained more inclusions. Figure 4B, D, and F showed the relief of the lath martensitic microstructure on the etched sample surface. With a high hardness, in the range of 410–450 $HV_{0.1}$, the weld metal phase was anticipated to be martensite. The equivalent content of Cr and Ni, according to the Schaeffler diagram (Ref. 31), is calculated in Table 5 from measured compositions with chemical analysis. The Cr_{eq} and Ni_{eq} of different weld metals in the Schaeffler diagram confirmed that the phase of the X65/1764 weld metal was martensite and all the 46200/1766 welds were martensite except one that had a small portion of retained austenite (Fig. 5). FeMnAl/1764 is austenite according to the Schaeffler diagram, and this explains its lowest hardness (183 $HV_{0.1}$), as shown in Table 3.

Toughness Test Results

Figure 6 shows the toughness data for different welds and base metals. The toughness of the four base metals tested at room temperature was in agreement with the respective specifications. For a given base metal, the welds made with shielding gas containing CO_2 had much lower toughness than those made without CO_2 in the shielding gas. For example, among the welds of 46100/1766 that were tested, those welds using shielding gases containing CO_2 — T3, T8, T9, and T16 — had low toughness (absorbed energy 17–29 J). Weld T5 (46100/1766, GTAW, 100% Ar) had the highest toughness among the 46100/1766 welds, with an absorbed energy of 121 J.

In Fig. 6, a comparison of T18 and T19 vs. T10 and T11, with the same filler wire, shows that the weld of base metal 12560 had a higher toughness than the weld of base metal 46100. Comparing T19 and T12, the weld metal using the 1766 filler wire had a higher toughness than the weld metal with 1764 filler wire. The toughness of almost all the LTPT weld metals slightly decreased when tested at temperatures of 0° and −40°C, but there was one exception: T6 (46100/1766, GMAW, 75% Ar 25% He); the toughness at lower temperature was a little higher than at room temperature — Fig. 6. The X65 base metal had the highest toughness. The toughness of the X65/1764 weld metals produced by GTAW-HW was higher than the toughness of the other weld metals — Fig. 6. The FeMnAl/1764 weld metals produced using both GMAW and GTAW also had relatively high toughness.

Figure 7 shows that the overall fracture surfaces of welds T3 (46100/1766, GMAW, 95% Ar 5% CO_2) and T16 (46100/1766, GMAW, 63% Ar 35% He 2% CO_2) were flat, and their fracture surfaces contained a large number of inclusions, each of which occupied a dimple or microvoid of the fracture surface — Fig. 7B, D. Welds T6 (46100/1766, GMAW, 75% Ar 25% He) and T13 (46100/1766, GTAW-HW, 100% Ar) did not use shielding gases containing CO_2. The fracture surfaces of T6 and T13 contained fewer and smaller inclusions than T3 and T16. Even though T6 was produced by GMAW, as were T3 and T16, the inclusions were much fewer because of the inert shielding gas that contained no CO_2 — Fig. 7F. Furthermore, their overall fracture surfaces were not as flat as those of T3 and T16. The uneven fracture surface is an indication of higher-absorbed energy to separate the weld or higher toughness.

Quantitatively, the sizes and amounts of inclusions in the 46100/1766 welds are shown in the Fig. 8 histograms, including welds T3, T16, T6, and T13 shown in Fig. 7. The fracture surface morphology as well as the inclusion size and distribution can explain the toughness sequence: T3 (17.33 J) < T16 (28.7 J) < T6 (58.33 J) < T13 (72.33 J) — Fig. 6. The T3, T8, T9, and T16 welds were created using GMAW with shielding gases containing CO_2. The T6 weld was made by GMAW with a 75% Ar 25% He shielding gas. The T5,

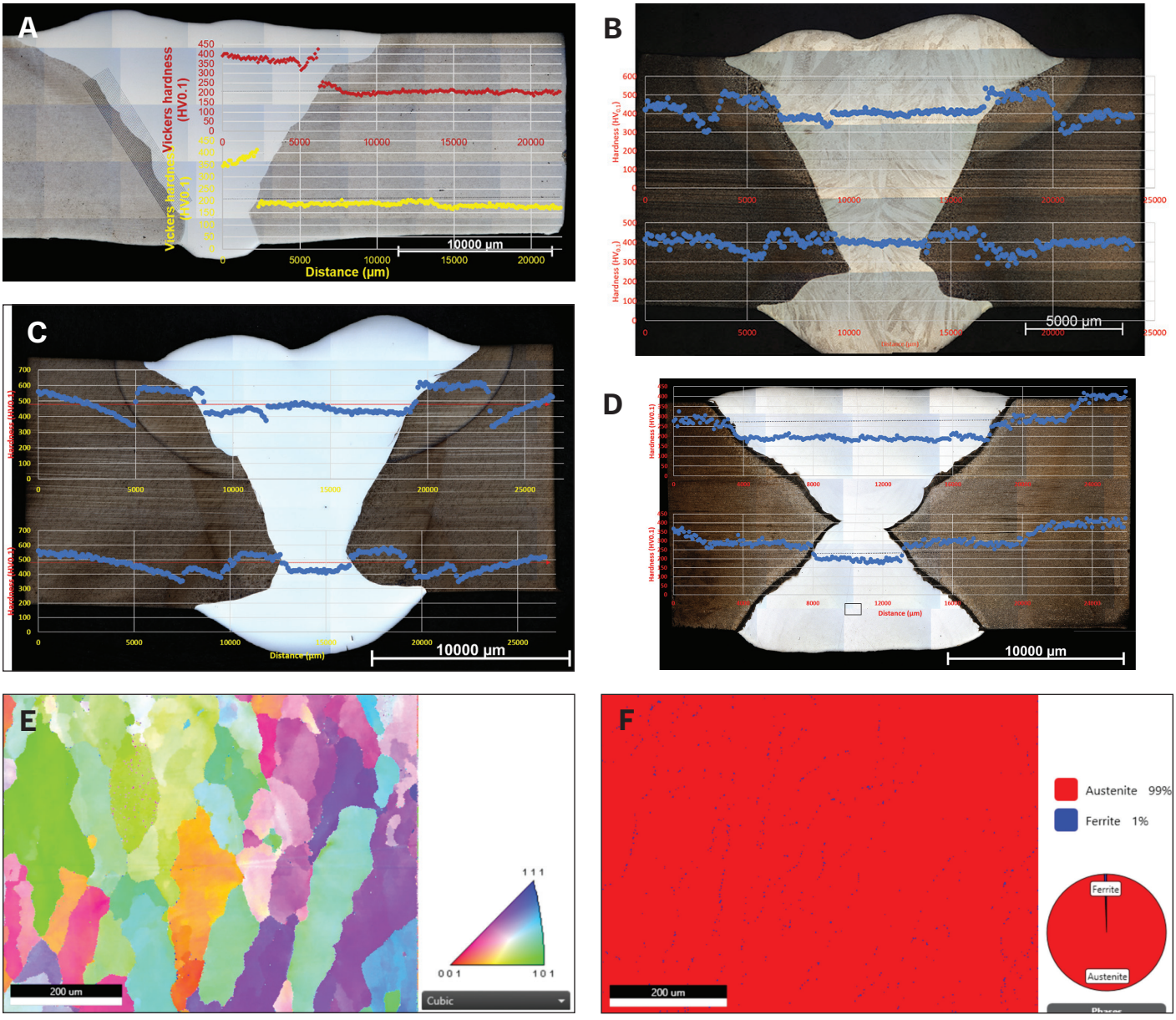

Fig. 3 — Hardness profiles of four welds: A — X65/1764; B — 12560/1764; C — 46100/1764; D — FeMnAl/1764, E — the inverse pole figure of the framed weld metal region of FeMnAl/1764 in D; F — the phase image of the selected weld metal region in D.

T13, and T17 welds were produced via GTAW or GTAW-HW with 100% Ar. The welds created using shielding gases containing CO_2 had more and larger inclusions.

Figure 9A shows a clear relationship between the number of inclusions per unit of area and the toughness. One set of data, indicated with blue dots, is from the 46100/1766 weld metals using various welding methods and shielding gases. Another set of data, indicated with orange diamonds, is from the X65 welds produced using different filler wires, welding methods, and shielding gases. The toughness decreased as the number of inclusions per unit of area increased. The blue dashed curve shows the trend with the 46100/1766 data. Figure 9B shows that the toughness decreased as the inclusion volume fraction increased. The inclusion size also influenced the toughness. The relationship is closer to being linear but the data are more scattered. The toughness decreased as the average inclusion size increased — Fig. 9C.

The inclusions were further analyzed using STEM. A typical inclusion specimen from weld T2 (46100/1764, GMAW, 95% Ar 5% CO_2) contained a single amorphous phase, as shown in Fig. 10A–C, especially in the diffraction pattern in Fig. 10C. Another inclusion specimen from weld T16 (46100/1766, GMAW, 63% Ar 35% He 2% CO_2) contained multiple phases (Fig. 10D–F). The diffraction pattern revealed that the major matrix phase (region 1) of the inclusion was amorphous (Fig. 10G), similar to Fig. 10C. The diffraction pattern as shown in Fig. 10H revealed the square

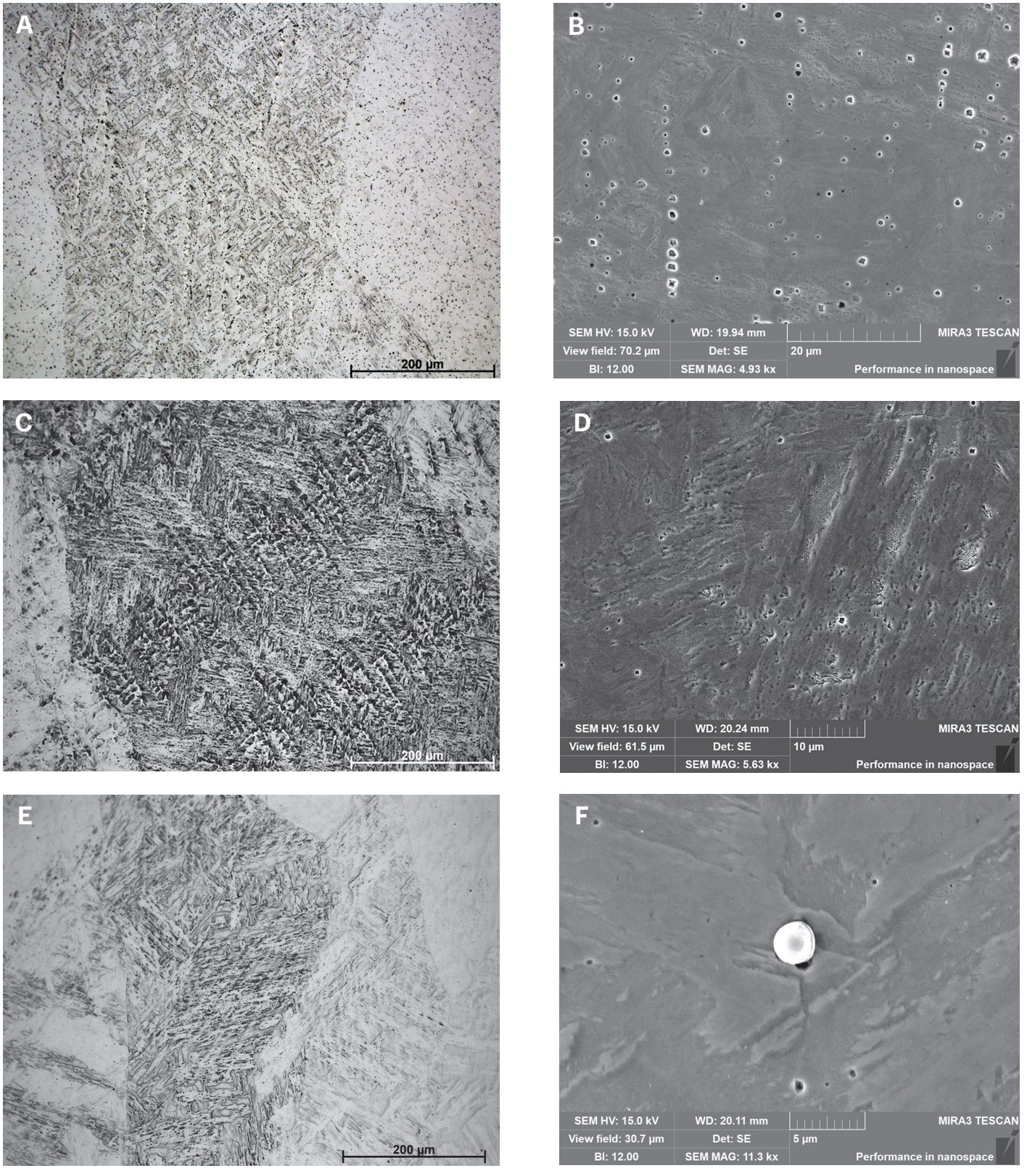

Fig. 4 — Images A, C, and E, respectively, are the microstructures of samples T3, T6, and T5 under optical microscopy with a scale bar of 200 mm. Images B, D, and F, respectively, are the higher-magnification microstructures of T3, T6, and T5 under SEM with scale bars of 20, 10, and 5 mm.

Table 2 — Typical Welding Conditions and Parameters (Weld T17)

Weld/Pass	1	2	3	4	5
Welding process	GTAW-HW manual/semiauto	GTAW-HW manual/semiauto	GTAW-HW manual/semiauto	GTAW-HW manual/semiauto	GTAW-HW manual/semiauto
Weld wire	1766	1766	1766	1766	1766
Shielding gas	100% Ar at 35 ft^3/h	100% Ar at 35 ft^3/h	100% Ar at 35 ft^3/h	100% Ar at 35 ft^3/h	100% Ar at 35 ft^3/h
Preheat/interpass temperature (°C)	N/A (23°C ambient)	<100°C	<100°C	<100°C	<100°C
Volts (V) max.	13.6	15.2	15.6	15.5	15.6
Amps (A)	210	325	325	300	300
Travel speed (in./min)	5.1	4.8	4.9	5.6	6.4

Table 2 (continued)

Weld/Pass	1	2	3	4	5
Net heat input from GTAW power supply ASME IX QW 409.1 (a) Joules/in. = (voltage × A ×60)/ (in./min)	33600	61750	62082	49821	43875
TIP TIG wire power supply HWa (A)	100	100	100	100	100
TIP TIG wire power supply HWv (V)	12	12	12	12	12
Additional heat input from wire power supply Joules/in. = (HWv∗HWa∗60)/ (in./min)	14118	15000	14694	12857	11250
Gross heat input (GTAW power supply and HW power supply) kJ = Joules/1000	47.7	76.8	76.8	62.7	55.1
Wire feed speed (in./min) automatic or machine only	70	120	138	120	120
String or weave, weave enter amplitude	Stringer	Weave 1/8	Weave 1/4	Stringer	Stringer

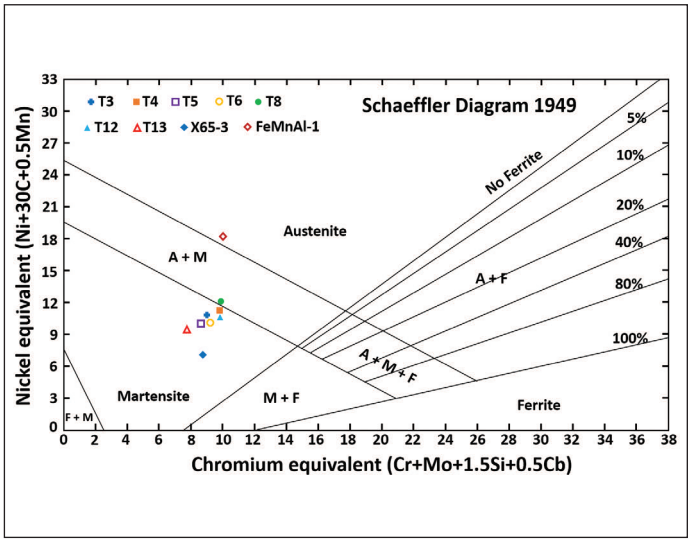

Fig. 5 — The Cr_{eq} and Ni_{eq} of the weld metals in the Schaeffler diagram indicating the phases of the weld metals (Ref. 31).

phase (region 2 in Fig. 10F) was spinel $Mn(Cr, Ti)_2O_4$. The diffraction pattern (Fig. 10H) was taken under the (Ref. 32) zone of the spinel.

The composition of the inclusions was revealed with the TEM/EDX analysis (Table 6 and Fig. 11). The TEM/EDX maps showed that the amorphous inclusion matrix (region 1) contained mainly the elements Al, Mn, O, and Si. The square phase (region 2) contained Al, Cr, Mn, Ti, and O. Regions 3 and 4 containing Cr, Mn, and Ti were the third phase. Region 5 containing Mn and S was the fourth phase, which should have been MnS. The general composition of the weld metal and the quantitative compositions of regions 1 and 2 are listed in Table 4. The compounds in region 1 of the inclusion should have been a mixture of MnO, SiO_2, and Al_2O_3 because the major elements in region 1 were O, Si, Mn, and Al — Fig. 11B–E. Thus, a key finding from this study was that the inclusions contained significant amounts of O, and the major source of O was from the shielding gas containing CO_2. This explains the significantly higher number of inclusions in the weld metal made with shielding gas containing CO_2 than those with the inert gases.

Discussion

Toughness of the Weld Metals

For armor steels, the LTPT weld metals made using GTAW or GTAW-HW with 100% Ar had high toughness in part because the weld metal was "clean" with minimal or few inclusions. The high hardness of ~ 410–450 $HV_{0.1}$, the lath microstructure, and the calculated Ni_{eq}/Cr_{eq} ratio according to the Schaeffler diagram (Ref. 31) showed that the weld metal was martensitic. The LTPT weld metals made using GTAW or GTAW-HW had favorable prop-

Table 3 — Hardness of Different Regions in the Selected Welds of Four Base Metals

Weld name	X65/1764	12560/1764	46100/1764	FeMnAl/1764
Welding method	GTAW-HW	GMAW	GMAW	GMAW
Shielding gas	100% Ar	95% Ar 5% CO_2	95% Ar 5% CO_2	75% Ar 25% He
Average hardness in the base metal ($HV_{0.1}$)	204	414	608	423
Average hardness in the weld metal ($HV_{0.1}$)	377	406	452	183
Average hardness in the HAZ ($HV_{0.1}$)	209	505	599	292
Lowest hardness in the HAZ ($HV_{0.1}$)	185	283	337	268

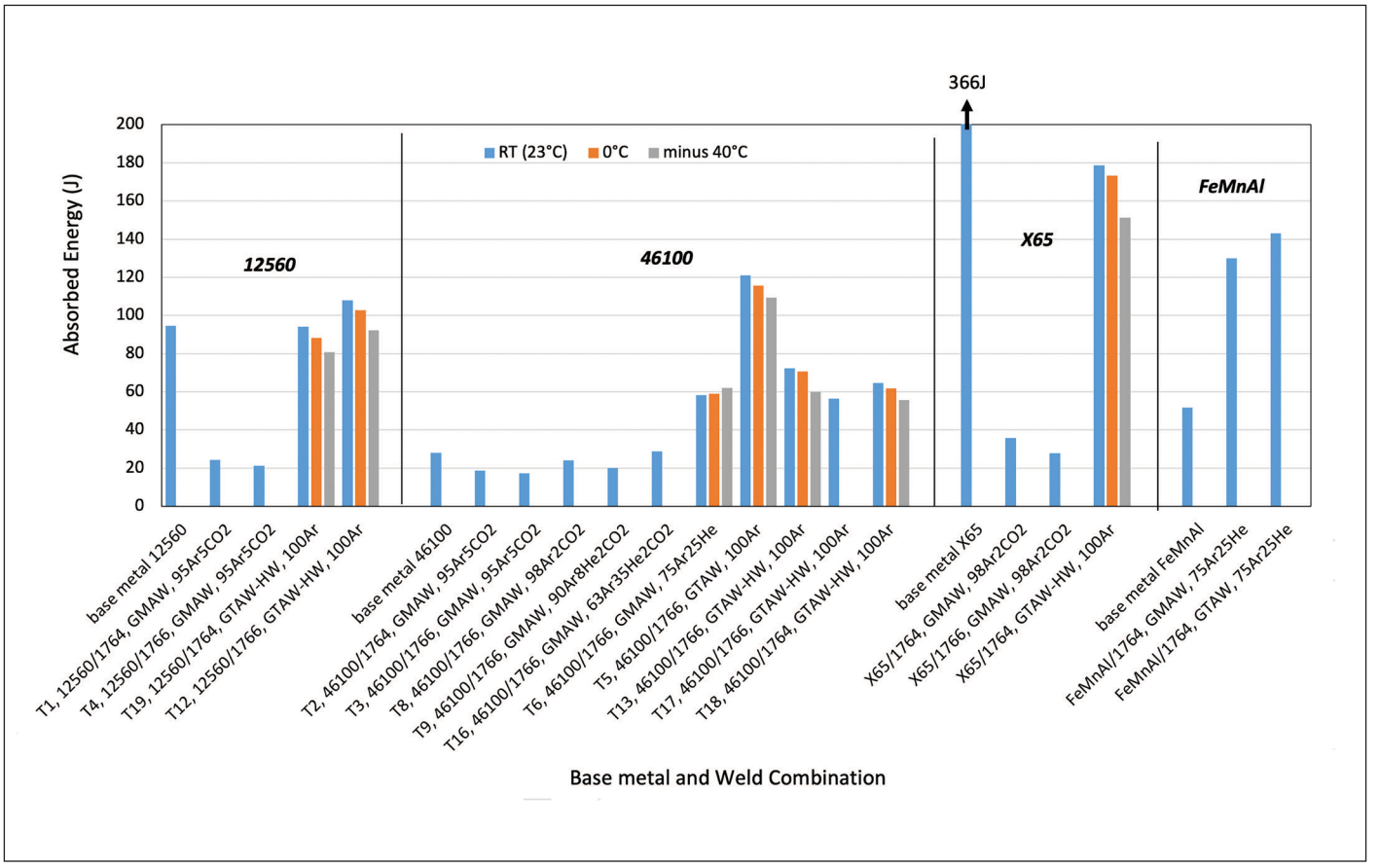

Fig. 6 — The toughness of base and weld metals in different conditions.

erties of high toughness and high strength. The high toughness may have resulted from depression of the M_s temperature and reduction of the tensile stresses as a result of the martensitic phase transformation.

However, when large amounts of inclusions formed in the weld metals, the toughness was compromised. When GMAW was used with an inert shielding gas like 75% Ar 25% He (T6), the weld toughness was high because the inert shielding gas did not promote the formation of oxide inclusions, and thus only a few small inclusions formed in the weld metal.

Other authors have reported that inclusions in the weld metal can promote the formation of acicular ferrite, which is desirable for increasing the weld metal toughness (Refs. 2, 3, 32). Acicular ferrite leads to high toughness because of its fine grain size, high dislocation density within the grains, high-angle grain boundaries, and interlocking structures (Ref. 4). These microstructures help resist crack formation and propagation. The formation of acicular ferrite in steel welds is influenced by the size and chemical compositions of the inclusions (Refs. 9, 32).

A high Ni_{eq}/Cr_{eq} ratio (Table 5) excluded the possibility of ferrite formation in LTPT weld metals. The influence of inclusions on toughness in LTPT weld metals was totally different from their influence on weld metals with acicular ferrite formation. Inclusions of a certain size assist the nucleation of acicular ferrite and increase toughness (Refs. 4, 33). In our study, the toughness decreased as the number of inclusions increased — Fig. 9A. The toughness also decreased as the volume fraction and sizes of inclusions increased — Fig. 9B, C. The inclusions in high-nickel and high-chromium LTPT weld metals assisted fracture propagation and thus reduced the toughness.

Figure 12 contains sketches of how inclusions assist crack propagation. At the front of the crack tip, there is a tensile stress field. The proximity of the crack tip is plasticized under the stress (Ref. 34). When the crack is propagating and about to reach the inclusion, the tensile stress field causes the detachment of the inclusion from the matrix material, causing the formation of a void around the inclusion before the crack reaches the inclusion — Fig. 12. The incoherent phase boundary results in weak bonding between the matrix material and the inclusion. The crack propagates and merges quickly into the preformed void. Compared with breaking the bond of the 100% matrix material, the energy required to break the bond between the inclusions and the matrix material is greatly reduced. Thus, the absorbed energy, an indicator of toughness, is greatly reduced. The preformed voids around the inclusions explain the fracture morphology of microvoids, or dimples with inclusions, in Fig. 7B and D. Each dimple was occupied by only one inclusion, not two or more inclusions, according to the formation mechanism. Some dimples were not occupied by inclusions because the inclusions may have been taken away during cracking or on the other side of the fracture surface.

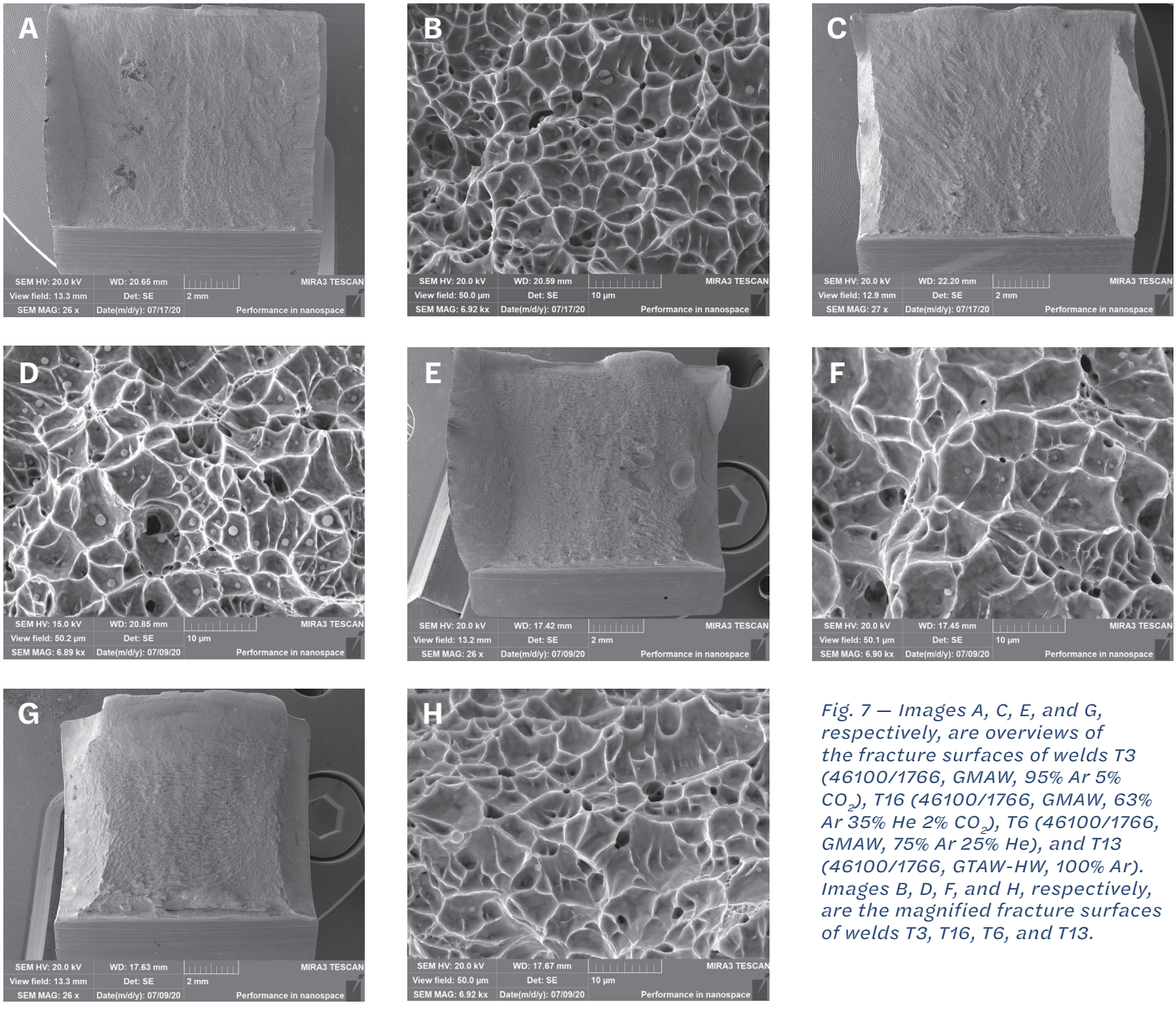

Fig. 7 — Images A, C, E, and G, respectively, are overviews of the fracture surfaces of welds T3 (46100/1766, GMAW, 95% Ar 5% CO_2), T16 (46100/1766, GMAW, 63% Ar 35% He 2% CO_2), T6 (46100/1766, GMAW, 75% Ar 25% He), and T13 (46100/1766, GTAW-HW, 100% Ar). Images B, D, F, and H, respectively, are the magnified fracture surfaces of welds T3, T16, T6, and T13.

Composition and Formation of the Inclusions

There were single-phase and multiple-phase inclusions in the LTPT weld metals. The TEM work showed that the major phase of the inclusions was noncrystalline amorphous compounds of Al_2O_3, MnO, and SiO_2. Even for inclusions containing multiple phases, the compounds Al_2O_3, MnO, and SiO_2 were the major phases. During welding, it was possible that some inclusions may have ascended toward the top of the weld metal (Ref. 32).

Shielding gases containing CO_2 were used in this study, and the CO_2 was the major source of oxygen in the weld metal. In the high-temperature arc environment, $CO_{2(g)} \rightarrow CO_{(g)} + O_{(g)}$. Ojima et al. (Ref. 35) and Meneses et al. (Ref. 36) reported CO generation from arc welding using CO_2. Their studies supported the hypothesis that CO_2 dissociates to CO and O during arc welding. Gaseous monoatomic oxygen transforms to dissolved oxygen by dissolving into the weld pool $O_{(g)} \rightarrow O_{(diss)}$. The free energy is $\Delta G = -88064 + 15.045T$ (Ref. 37). The free energy equation revealed that as the temperature increased, there was less gaseous monoatomic oxygen dissolving into the weld metal. Therefore, the power source, heat input, and shielding gas type were assumed to be significant factors in influencing the dissolution of oxygen and thus the formation of inclusions (oxides). More investigation is needed to confirm this hypothesis.

The Marangoni convection, buoyancy, and electromagnetic forces cause intense circulation and stirring in the weld pool for single-bead arc welding (Refs. 32, 38, 39). The dissolved oxygen has sufficient opportunity to interact with the deoxidizing elements and form oxide inclusions. The following are standard free energy equations for the formation of different oxides:

$Fe + O_{(diss)} \rightarrow FeO_{(liq)}$, $\Delta G = -33{,}200 + 13.52T$ (Refs. 40–42)

$2Al + 3O_{(diss)} \rightarrow Al_2O_{3(s)}$, $\Delta G = -289{,}060 + 93.52T$ (Refs. 40–42)

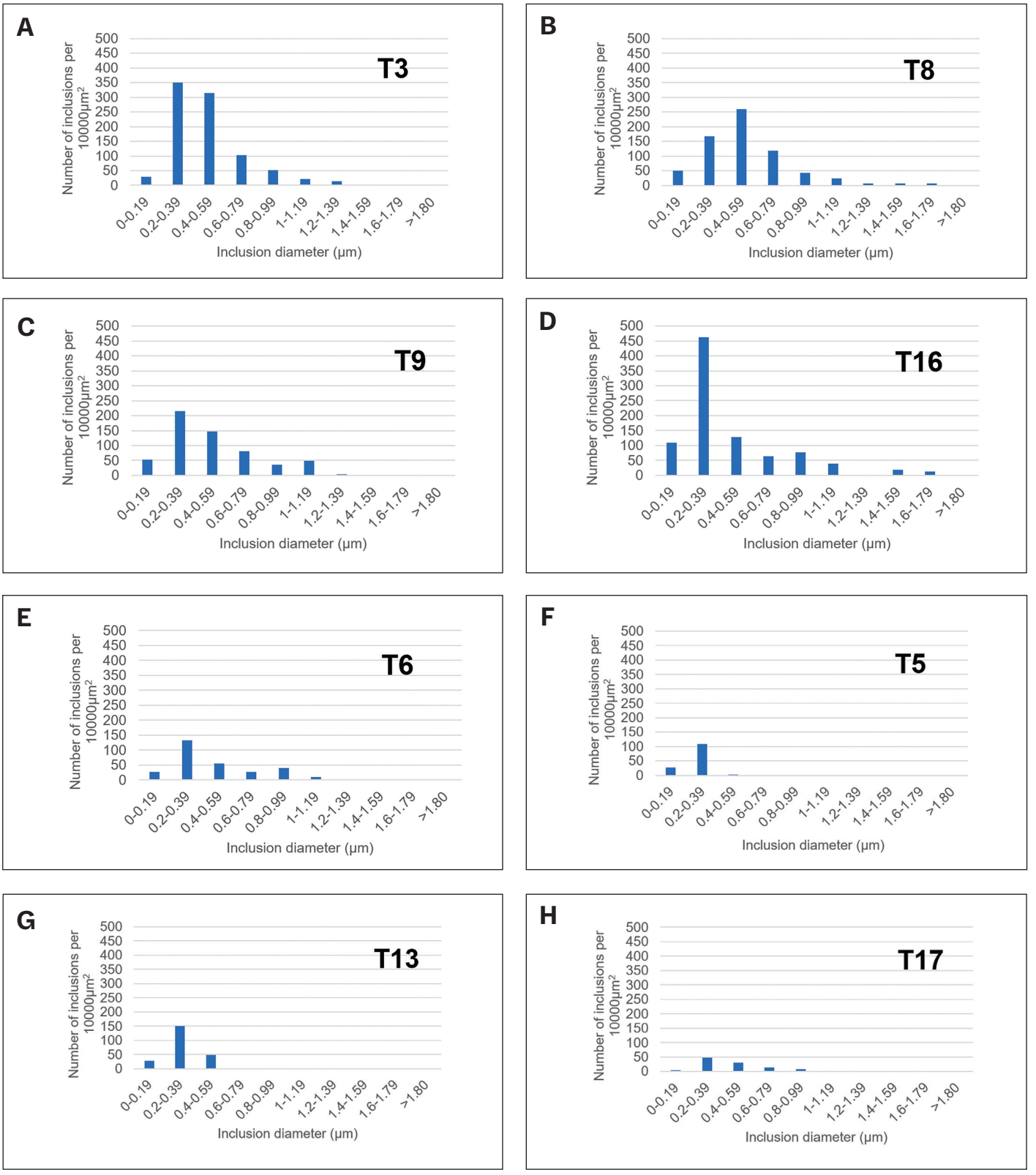

Fig. 8 — The size distribution of inclusions in welds: A — T3 (46100/1766, GMAW, 95% Ar 5% CO_2); B — T8 (46100/1766, GMAW, 98% Ar 2% CO_2); C — T9 (46100/1766, GMAW, 90% Ar 8% He 2% CO_2); D — T16 (46100/1766, GMAW, 63% Ar 35% He 2% CO_2); E — T6 (46100/1766, GMAW, 75% Ar 25% He); F — T5 (46100/1766, GTAW, 100% Ar); G — T13 (46100/1766, GTAW-HW, 100% Ar); H — T17 (46100/1766, GTAW-HW, 100% Ar).

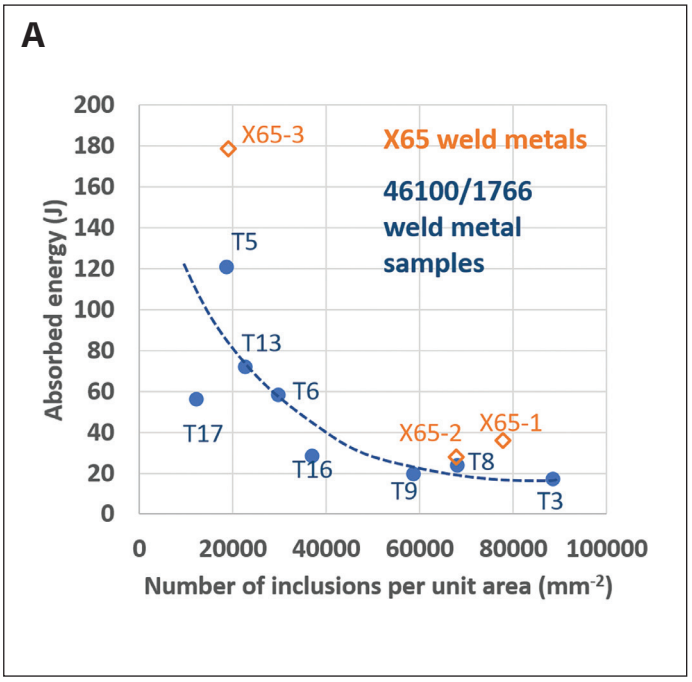

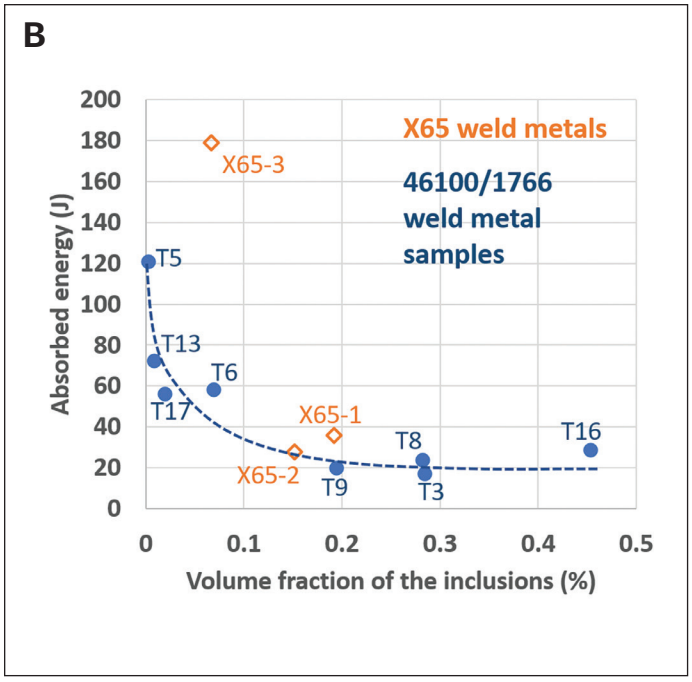

$2Ti + 3O_{(diss)} \rightarrow Ti_2O_{3(s)}$, $\Delta G = -87{,}560 + 29.14T$ (Refs. 41–43)

$Si + 2O_{(diss)} \rightarrow SiO_{2(s)}$, $\Delta G = -140{,}950 + 54.62T$ (Refs. 41–43)

$Mn + O_{(diss)} \rightarrow MnO_{(s)}$, $\Delta G = -68{,}816 + 29.95T$ (Refs. 41–43)

Even though the major element in the weld metal is iron, $Fe + O_{(diss)} \rightarrow FeO_{(liq)}$ will form. However, Al, Si, Mn, Ti, and so on are all stronger deoxidizing elements and can deprive oxygen (Refs. 40–42). For example, $3FeO_{(liq)} + 2Al \rightarrow Al_2O_{3(s)} + 3Fe$, $\Delta G = -189{,}460 + 52.96T$ (Refs. 40–42).

According to the standard free energy equations for the formation of different oxides shown above (Refs. 44–46), the reactions theoretically occur in a sequence to form the phases in the inclusions (Ref. 32). The sequence of phases formed may be different. Theoretically, inclusions with multiple compounds or phases should have a layered structure. The core region should be Al_2O_3, then the outer layer should be respectively Ti_2O_3, SiO_2, MnO, and TiN; and MnS should be on the outermost layer of the inclusion. Some authors (Refs. 47–49) did find a layered structure in oxides and confirmed this inference. In the inclusion shown in Figs. 10 and 11, the authors did not characterize the layer structure in the amorphous phase of the different oxides. It is more likely that the Al_2O_3, SiO_2, and MnO are homogeneously mixed. Some other authors' (Refs. 9, 50) results did not show a layered structure for the oxides in inclusions. However, the authors of this paper did find MnS (region 5) on the outermost surface of the inclusion, partially covering the inclusion, as shown in Fig. 11D and J, as well as regions 3–5 in Fig. 11A. The diffraction pattern of region 2 (Fig. 10F, H) showed that the phase should be a spinel phase $(Mn, Cr)(Ti, V)_2(O, N)_4$ (Refs. 49, 51).

Franklin (Ref. 44) proposed that the volume fractions of inclusions could be calculated using an empirical equation, $V_v = 10^{-2} * [5.0 * (\%O) + 5.4 * (\%S - 0.003)]$, where V_v is the volume fraction of the inclusion and %O and %S are the oxygen and sulfur content, respectively. This relationship needs to be confirmed with more data. This study supports that a higher CO_2 content in the

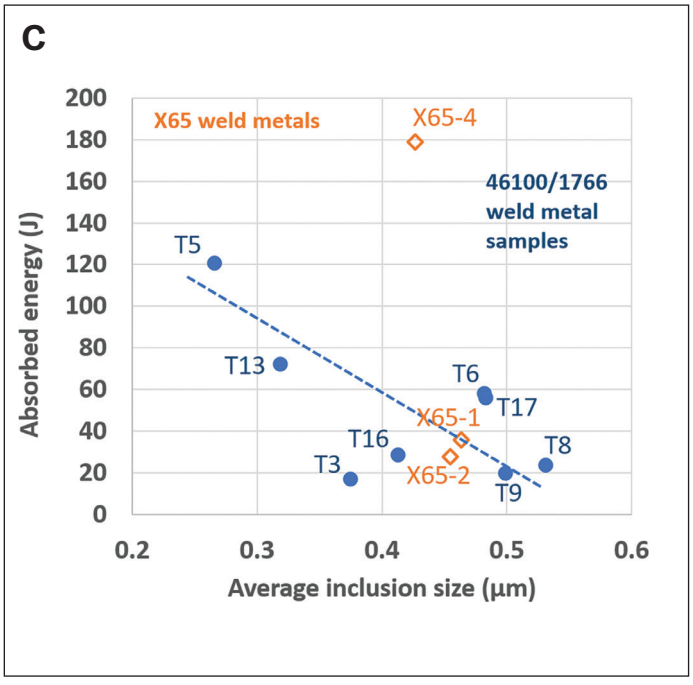

Fig. 9 — A — The relationship between the inclusion population density and toughness; B — the relationship between the volume fraction of the inclusions and the toughness; C — the relationship between the average inclusion size and toughness. The data are for welds T3 (46100/1766, GMAW, 95% Ar 5% CO_2), T8 (46100/1766, GMAW, 98% Ar 2% CO_2), T9 (46100/1766, GMAW, 90% Ar 8% He 2% CO_2), T16 (46100/1766, GMAW, 63% Ar 35% He 2% CO_2), T6 (46100/1766, GMAW, 75% Ar 25% He), T5 (46100/1766, GTAW, 100% Ar), T13 (46100/1766, GTAW-HW, 100% Ar), and T17 (46100/1766, GTAW-HW, 100% Ar).

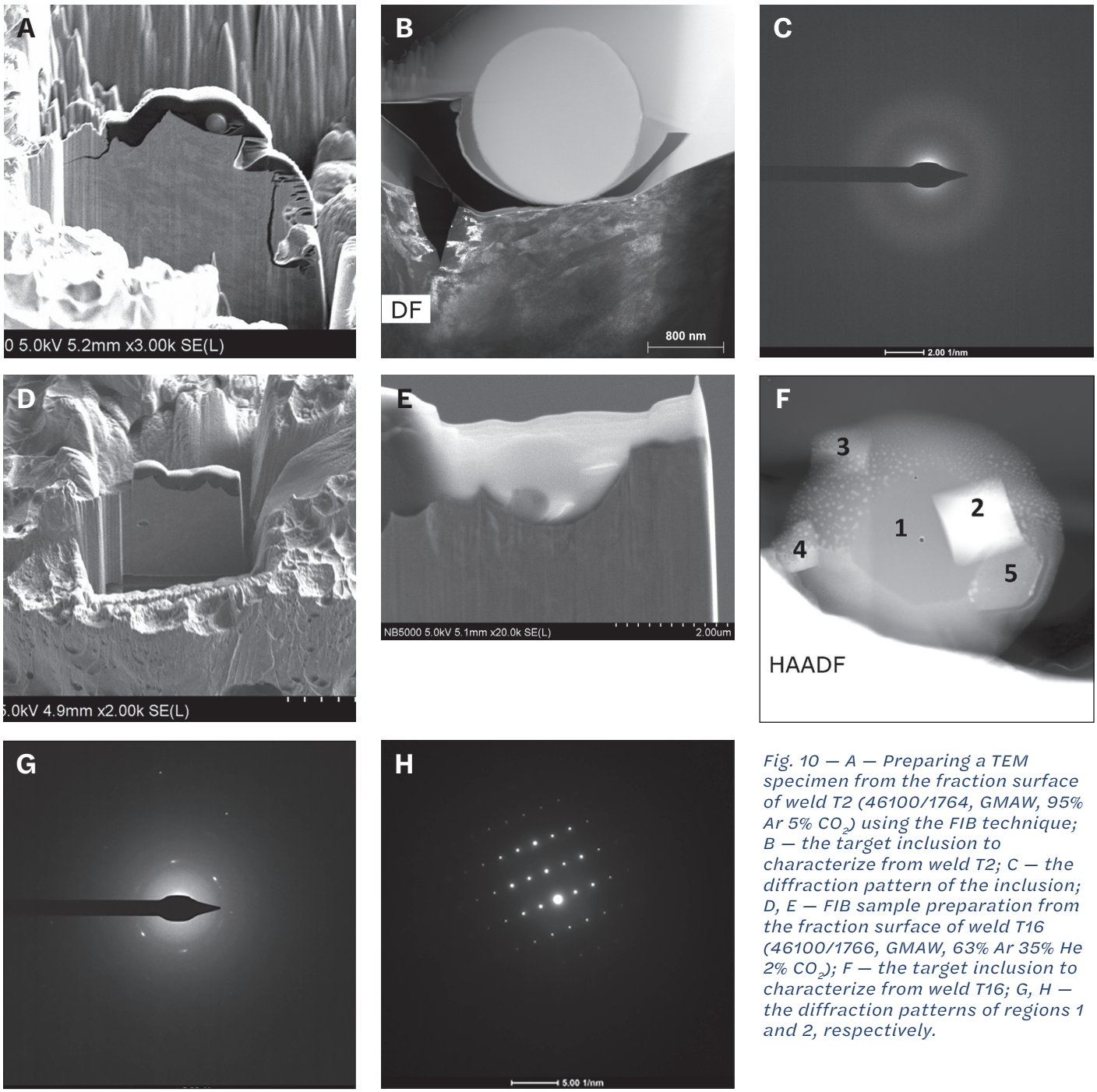

Fig. 10 — A — Preparing a TEM specimen from the fraction surface of weld T2 (46100/1764, GMAW, 95% Ar 5% CO_2) using the FIB technique; B — the target inclusion to characterize from weld T2; C — the diffraction pattern of the inclusion; D, E — FIB sample preparation from the fraction surface of weld T16 (46100/1766, GMAW, 63% Ar 35% He 2% CO_2); F — the target inclusion to characterize from weld T16; G, H — the diffraction patterns of regions 1 and 2, respectively.

shielding gas results in a higher volume of inclusions in the weld metal. This conclusion is confirmed by the results shown in Fig. 9.

Conclusion

The root causes of the relatively low toughness of LTPT weld metals made by GMAW with shielding gases containing CO_2 were investigated. It was found that, for high-strength steel welds with predominately martensite microstructures, oxide inclusions were the primary factor resulting in relatively low toughness. The formation of these oxide inclusions was associated with the presence of oxygen, which formed under the welding arc from the dissociation of CO_2 in the shielding gases that are commonly used in GMAW of structural steels. For the steel and weld wires studied in this work, eliminating oxygen or CO_2 in the shielding gas greatly reduced the oxide inclusions, resulting in significant increases in the weld metal toughness so that it matched the base metal toughness. More specifically,

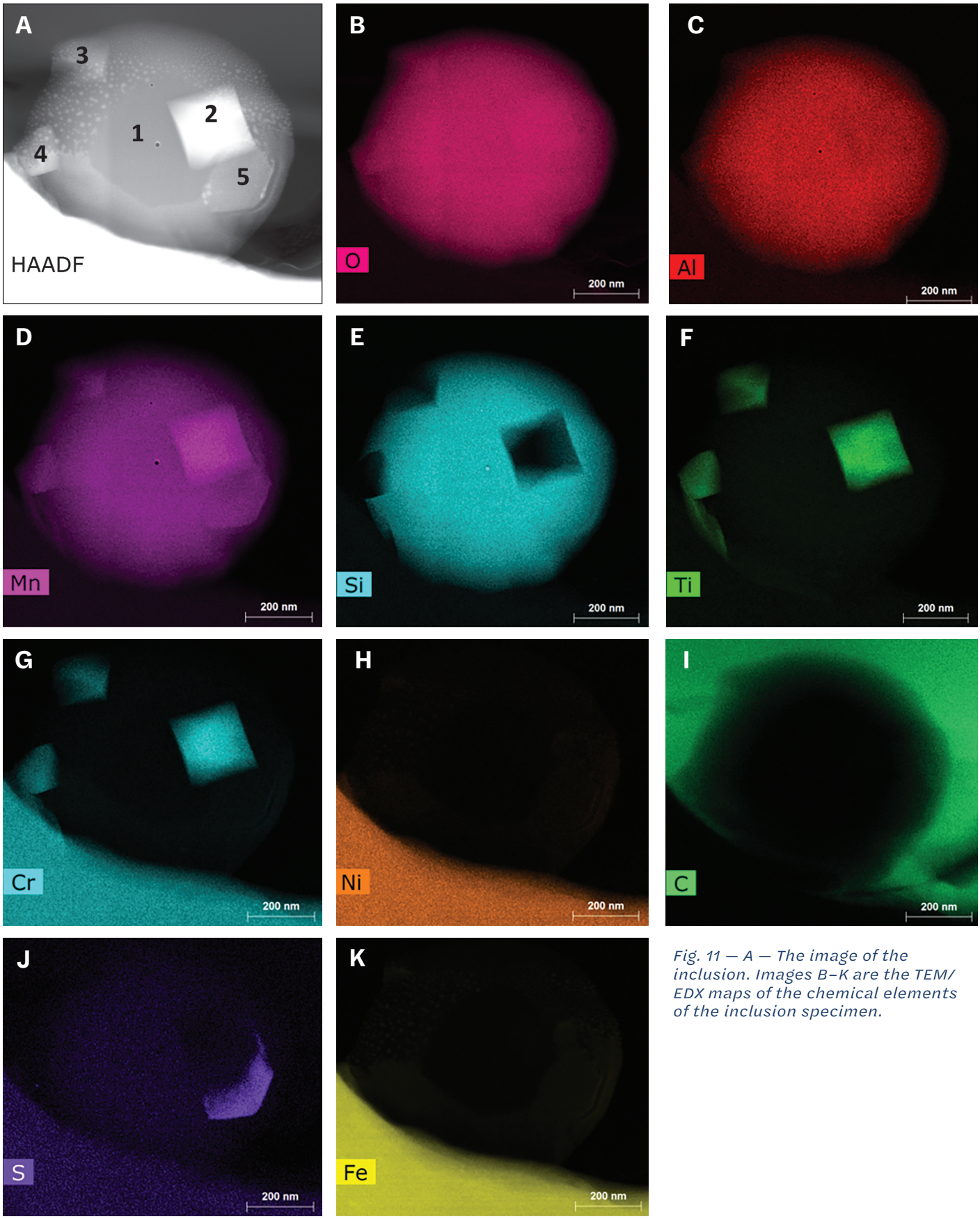

Fig. 11 — A — The image of the inclusion. Images B–K are the TEM/EDX maps of the chemical elements of the inclusion specimen.

1) Inclusions in the weld metal promoted the propagation of cracks through the weld metal and thus decreased the toughness. Crack propagation around inclusions resulted in a microvoid or dimple fracture morphology.

2) The weld metal toughness decreased with an increase in the number of inclusions per unit of area, in the volume fraction of the inclusions, or in the inclusion size.

3) GMAW with shielding gases containing CO_2 produced weld metals with oxide inclusions. The major compounds of the inclusions were Al_2O_3, SO_2, and MnO. They were amorphous non-crystalline phases. Certain inclusions contained other phases, such as MnS and/or spinel phase.

4) GMAW with inert shielding gas 75% Ar 25% He as well as GTAW and GTAW-HW with 100% Ar produced weld metals with far fewer inclusions than GMAW with shielding gases containing CO_2.

5) Dilution between the welding wire and base metal greatly influenced the LTPT weld metal strength. The LTPT welding wires used in this study worked well to produce high-strength (as evidenced by the high hardness) and high-toughness martensite weld metal for the three structure steels with hardness levels generally matching the base metal hardness. On the other hand, the high Mn and Al content of FeMnAl steel resulted in a relatively low hardness austenitic microstructure in the weld metal.

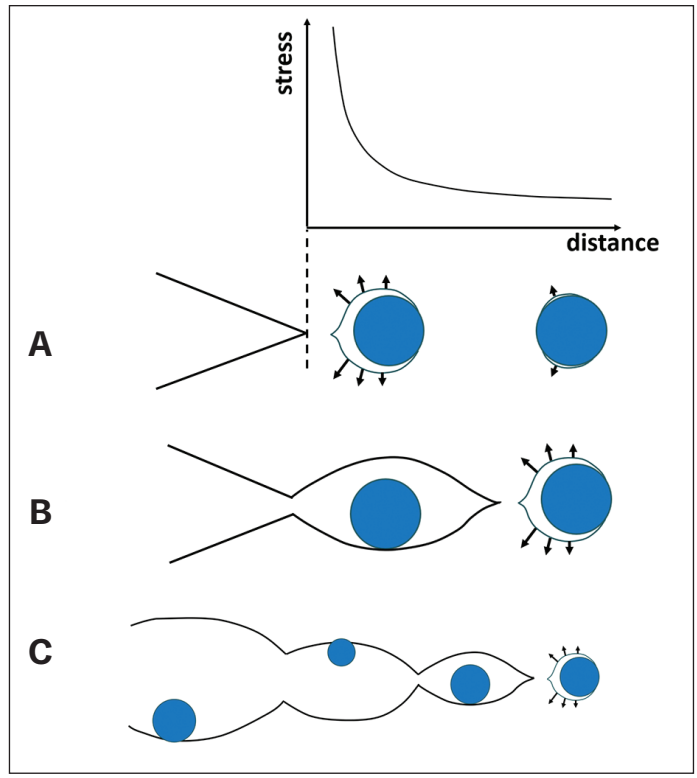

Fig. 12. — Cracking propagation assisted by inclusions. A–C are different stages of the crack propagation.

Table 4 — Hardness of Different Regions in Different 46100/1766 Welds

Weld name	T3	T8	T9	T16	T6	T5	T13	T17
Welding method	GMAW	GMAW	GMAW	GMAW	GMAW	GTAW	GTAW-HW	GTAW-HW
Shielding gas	95% Ar 5% CO_2	98% Ar 2% CO_2	90% Ar 8% He 2% CO_2	63% Ar 35% He 2% CO_2	75% Ar 25% He	100% Ar	100% Ar	100% Ar
Average hardness in the weld metal ($HV_{0.1}$)	414	435	449	461	407	417	411	427
Average hardness in the HAZ ($HV_{0.1}$)	580	581	596	599	595	562	583	590
Lowest point at over tempered zone ($HV_{0.1}$)	337	341	337	341	350	329	333	337

Table 5 — Chemical Analysis of Selected Weld Metals and Equivalent Cr and Ni Content According to the

		Al	C	Co	Cr	Cu	Fe	Mn	Mo
T3	46100/1766, GMAW, 95% Ar 5% CO_2	0.01	0.08	<0.01	8.32	0.02	81.76	0.70	0.21
T8	46100/1766, GMAW, 98% Ar 2% CO_2	<0.01	0.08	<0.01	9.06	0.01	80.32	0.67	0.17
T6	46100/1766, GMAW, 75% Ar 25% He	0.01	0.06	<0.01	8.35	0.02	81.73	0.74	0.20
T5	46100/1766, GTAW, 100% Ar	0.01	0.08	<0.01	7.41	0.03	83.47	0.75	0.24
T13	46100/1766, GTAW-HW, 100% Ar	0.01	0.09	<0.01	6.79	0.02	85.01	0.60	0.17
T4	12560/1766, GMAW, 95% Ar 5% CO_2	0.01	0.065	0.02	8.89	0.02	80.50	1.00	0.23
T12	12560/1766, GTAW-HW, 100% Ar	0.01	0.045	0.015	8.86	0.015	80.58	0.99	0.225
X65-3	X65/1764, GTAW-HW, 100% Ar	0.02	0.04	0.01	7.70	0.05	85.09	0.71	0.42
FeMnAl-1	FeMnAl/1764 GMAW, 75% Ar 25% He	2.10	0.265	0.01	8.56	0.04	73.19	8.70	0.59

Acknowledgments

This work was supported by the U.S. Army Combat Capabilities Development Command Ground Vehicle Systems Center (DEVCOM GVSC) and the Department of Energy's Fossil Energy Technology Office. The authors acknowledge the assistance of Weicheng Zhong, Chad Parish, and Dorothy Coffey of Oak Ridge National Laboratory for the TEM work.

Schaeffler Diagram (Ref. 31)								
Ni	**O**	**P**	**S**	**Se**	**Si**	**Zn**	**Cr_{eq}**	**Ni_{eq}**
8.51	0.05	<0.005	0.001	<0.01	0.34	<0.01	9.04	11.26
9.32	0.04	<0.005	0.001	<0.01	0.33	<0.01	9.73	12.06
8.50	0.01	<0.005	0.001	<0.01	0.38	<0.01	9.12	10.67
7.63	< 0.01	<0.005	0.001	<0.01	0.38	<0.01	8.22	10.41
6.98	0.01	<0.005	0.001	<0.01	0.32	<0.01	7.44	9.98
8.82	0.05	<0.005	0.0015	<0.01	0.395	<0.01	9.72	11.27
8.81	0.01	<0.005	0.002	<0.01	0.45	<0.01	9.76	10.66
5.59	0.01	<0.005	0.001	<0.01	0.37	<0.01	8.675	7.145
6.03	0.005	<0.005	0.001	<0.01	0.535	<0.01	9.953	18.33

Table 6 — Chemical Compositions of the Inclusion Matrix (Region 1) and the Square Phase (Region 2) as well as the General Chemical Composition of the Weld Metal

Wt-%	O	Si	Mn	Mn	Ti	C	Fe	Cr	Ni	S
Region 1	37.7	21.1	29.6	7.6	1.4	0.35	0.82	0.96	0	0.43
Region 2	27.0	2.28	27.59	5.0	15.9	0.76	1.87	19.7	0	0
General composition of the weld metal	0.04	0.33	0.67	< 0.01	—	0.08	80.32	9.06	9.32	0.001

References

1. American Petroleum Institute. 2012. *API SPEC 5: Specification for Line Pipe*, p. 34–36.

2. Abson, D. J., and Pargeter, R. J. 1986. Factors influencing as-deposited strength, microstructure, and toughness of manual metal arc welds suitable for C-Mn steel fabrications. *International Metals Reviews* 31(1): 141–196. DOI: 10.1179/imtr.1986.31.1.141

3. Farrar, R. A., and Harrison, P. L. 1987. Acicular ferrite in carbon-manganese weld metals: An overview. *Journal of Materials Science,* p. 3812–3820. DOI: 10.1007/BF01133327

4. Zhang, T., Li, Z., Kou, S., Jing, H., Li, G., Li, H., and Kim, H. J. 2015. Effect of inclusions on microstructure and toughness of deposited metals of self-shielded flux cored wires. *Materials Science & Engineering A* 628: 332–339. DOI: 10.1016/j.msea.2015.01.070

5. Lan, L., Kong, X., Qiu, C., and Zhao, D. 2016. Influence of microstructural aspects on impact toughness of multi-pass submerged arc welded HSLA steel joints. *Materials and Design* 90: 488–498. DOI: 10.1016/j.matdes.2015.10.158

6. Sugden, A. A. B., and Bhadeshia, H. K. D. H. 1989. Lower acicular ferrite. *Metallurgical Transactions A* 20(9): 1811–1818. DOI: 10.1007/BF02663212

7. Bhadeshia, H. K. D. H., and Christian, J. W. 1990. Bainite in steels. *Metallurgical Transactions A* 21: 767–797. DOI: 10.1007/BF02656561

8. Babu, S. S., and Bhadeshia, H. K. D. H. 1991. Mechanism of the Transition from Bainite to Acicular Ferrite. *Materials Transactions JIM* 32(8): 679–688. DOI: 10.2320/matertrans1989.32.679

9. Lee, T.-K., Kim, H. J., Kang, B. Y., and Hwang, S. K. 2000. Effect of inclusion size on the nucleation of acicular ferrite in welds. *ISIJ International* 40(12): 1260–1268. DOI: 10.2355/isijinternational.40.1260

10. Abson, D. J., and Dolby, R. E. 1980. International Institute of Welding Document IXJ-29-80.

11. Grong, O., and Matlock, D. K. 1986. Microstructural development in mild and low-alloy steel weld metals. *International Metals Reviews* 31(1): 27–48. DOI: 10.1179/imtr.1986.31.1.27

12. Divya, M., Das, C. R., Mahadevan, S., Albert, S. K., Pandian, R., Kar, S. K., Bhaduri, A. K., and Jayakumar, T. 2015. Influence of PWHT on toughness of high chromium and nickel containing martensitic stainless steel weld metals. *Metallurgical and Materials Transactions A* 46: 2554–2567. DOI: 10.1007/s11661-015-2847-y

13. Norstrom, L. A., and Vingsbo, O. 1979. Influence of nickel on toughness and ductile-brittle transition in low-carbon martensite steels. *Metal Science* 13(12): 677–684. DOI: 10.1179/030634579790434321

14. Cao, R., Zhang, X. B., Wang, Z., Peng, Y., Du, W. S., Tian, Z. L., and Chen, J. H. 2014. Investigation of microstructural features determining the toughness of 980 MPa bainitic weld metal. *Metallurgical and Materials Transactions A* 45(2): 815–834. DOI: 10.1007/s11661-013-2020-4

15. Qiu, H., Terumi, N., Linning, W., Chengduo, W., and Kazuo, H. 2013. Impact behavior of 980 MPa grade Cr-Ni weld metal composed of martensite and retained austenite. *Quarterly Journal of the Japan Welding Society* 31(3): 216–221. DOI: 10.2207/qjjws.31.216

16. Keehan, E., Andrén, H. O., Karlsson, L., Murugananth, M., and Bhadeshia, H. K. D. H. 2002. Microstructural and mechanical effects of nickel and manganese on high strength steel weld metals. Retrieved on February 16, 2021, from *researchgate.net/publication/237244420_Microstructural_and_mechanical_effects_of_nickel_and_manganese_on_high_strength_steel_weld_metals*.

17. Keehan, E., Karlsson, L., and Andren, H.-O. 2006. Influence of carbon, manganese and nickel on microstructure and properties of strong steel weld metals: Part 1 — Effect of nickel content. *Science and Technology of Welding and Joining* 11(1): 1–8. DOI: 10.1179/174329306X77830

18. Zhang, W., Zhong, Z., and Kang, S. 2015. Microstructures and mechanical properties of a martensitic steel welded with flux-cored wires. *International Journal of Coal Science & Technology* 2(3): 254–260. DOI: 10.1007/s40789-015-0082-1

19. Barrick, E. J., and DuPont, J. N. 2020. Microstructural characterization and toughness evaluation of 10-wt% Ni steel weld metal gas tungsten arc and gas metal arc weld fusion zones. *Materials Science & Engineering A* 796: 1–19. DOI: 10.1016/j.msea.2020.140043

20. Jones, W. K. C., and Alberry, P. J. 1977. A model for stress accumulation in steels during welding. *Metal Technology* 11: 557–566.

21. Yue, X., Feng, X., and Lippold, J. C. 2013. Quantifying heat-affected zone hydrogen-induced cracking in high-strength naval steels. *Welding Journal* 92(9): 265-s to 273-s.

22. Dodge, M. F., Dong, H. B., and Gittos, M. F. 2014. Effect of post-weld heat treatment on microstructure evolution in dissimilar joints for subsea oil and gas systems. *Materials Research Innovations* 18(4): S4-907 to S4-913. DOI: 10.1179/1432891714Z.000000000807

23. Akiyama, E., Wang, M., Li, S., Zhang, Z., Kimura, Y., Uno, N., and Tsuzaki, K. 2013. Studies of evaluation of hydrogen embrittlement property of high-strength steels with consideration of the effect of atmospheric corrosion. *Metallurgical and Materials Transactions A* 44(3): 1290–1300. DOI: 10.1007/s11661-012-1403-2

24. Dai, T., and Lippold, J. C. 2018. The effect of postweld heat treatment on hydrogen assisted cracking of F22/Alloy 625 overlays. *Welding Journal* 97(3): 75-s to 90-s.

25. Feng, Z. 2019. Repair welding technology for oil/gas pipelines. Unpublished work. Oak Ridge National Laboratory.

26. Du, W., Peng, Y., Xiao, H., He, C., and Tian, Z. 2010. Microstructure and toughness of 1000 MPa high strength weld metal. *Materials Science Forum* 638–642: 3441–3446. Switzerland. DOI: 10.4028/www.scientific.net/MSF.638-642.3441

27. Gianetto, J. A., Goodall, G. R., Tyson, W. R., Fazeli, F., Quintana, M., Rajan, A. V. B., and Chen, Y. 2012. Microstructure and properties of high strength steel weld metals. *Proceedings of the 2012 9th International Pipeline Conference,* pp. 515–526. New York, N.Y.: ASME. DOI: 10.1115/IPC2012-90526

28. U. S. Army Research Laboratory. 2019. MIL-DTL-12560K, *Armor Plate, Steel, Wrought, Homogeneous for Use in Combat Vehicles and for Ammunition Testing*. Defense Logistics Agency.

29. Frommeyer, G., and Brux, U. 2006. Microstructures and mechanical properties of high-strength Fe-Mn-Al-C Light-Weight TRIPLEX steels. *Steel Research International* 77(9–10): 627–633. DOI: 10.1002/srin.200606440

30. ASTM International. 2018. ASTM E23 — 18*, Standard Test Methods for Notched Bar Impact Testing of Metallic Materials*. West Conshohocken, Pa.: ASTM International.

31. Lippold, J. C., and Kotecki, D. J. 2005. *Welding Metallurgy and Weldability of Stainless Steels*. Hoboken, N.J.: John Wiley & Sons.

32. Babu, S. S., David, S. A., Vitek, J. M., Mundra, K., and DebRoy, T. 1995. Development of macro- and microstructures of carbon-manganese low alloy steel welds: Inclusion formation. *Materials Science and Technology* 11(2): 186–199. DOI: 10.1179/mst.1995.11.2.186

33. Jiang, Q. L., Li, Y. J., Wang, J., and Zhang, L. 2011.Effects of inclusions on formation of acicular ferrite and propagation of crack in high strength low alloy steel weld metal. *Materials Science and Technology* 27(10): 1565–1569. DOI: 10.1179/026708310X12815992418535

34. Recho, N. 2012. *Fracture Mechanics and Crack Growth*. London, UK: ISTE Ltd. and Hoboken, N.J.: John Wiley & Sons. DOI: 10.1002/9781118387184

35. Ojima, J. 2013. Generation rate of carbon monoxide from CO_2 arc welding. *Journal of Occupation Health* 55(1): 39–42. DOI: 10.1539/joh.12-0180-BR

36. Alves de Meneses, V., Silva Leal, V., and Scotti, A. 2016. Influence of metal transfer stability and shielding gas composition on CO and CO_2 emissions during short-circuiting MIG/MAG welding. *Soldagem & Inspeção* 21(3): 253–268. DOI: 10.1590/0104-9224/SI2103.02

37. Mundra, K., and DebRoy, T. 1993. Unpublished work. The Pennsylvania State University, Pa.

38. DebRoy, T., and David, S. A. 1995. Physical processes in fusion welding. *Reviews of Modern Physics* 67(1): 86–112. DOI: 10.1103/RevModPhys.67.85

39. David, S. A., and DebRoy, T. 1992. Current issues and problems in welding science. *Science* 257(5069): 497–502.

40. Turpin, M. L., and Elliott, J. F. 1966. Nucleation of oxide inclusions in iron melts. *JISI*, pp. 217–225. DOI: 10.1126/science.257.5069.497

41. Elliot, J. F., Gleiser, M., and Ramakrishna, V. 1963. *Volume II Thermodynamic and Transport Properties*. Boston, Ma.: Addison-Wesley.

42. Sigworth, G. K., and Elliott, J. F. 1974. The thermodynamics of liquid dilute iron alloys. *Metal Science* 8(1): 298–310. DOI: 10.1179/msc.1974.8.1.298

43. Turkdogan, E. T. 1980. *Physical Chemistry of High Temperature Technology*. New York, N.Y.: Academic Press.

44. Franklin, A. G. 1969. Comparison between a quantitative microscope and chemical methods for assessment of non-metallic inclusions. *Journal of The Iron and Steel Institute,* pp. 181–186.

45. Bailey, N., and Pargeter, R. J. 1988. The influence of flux type on the strength and toughness of submerged arc weld metal. The Welding Institute, Abington, UK.

46. Bhadeshia, H. K. D. H., and Svensson, L. E. 1993. *Mathematical Modelling of Weld Phenomena*. Eds. H. Cerjak and K. E. Easterling. London, UK: The Institute of Materials.

47. Kluken, A. O., and Grong, O. 1989. Mechanisms of inclusion formation in AI-Ti-Si-Mn deoxidized steel weld metals. *Metallurgical Transactions A* 20: 1335–1349. DOI: 10.1007/BF02665492

48. Seo, J. S., Lee, C., and Kim, H. J. 2013. Influence of oxygen content on microstructure and inclusion characteristics of bainitic weld metals. *ISIJ International* 53(2): 279–285. DOI: 10.2355/isijinternational.53.279

49. Seo, K., Kim, Y.-M., Kim, H. J., and Lee, C. 2015. Characterization of inclusions formed in Ti-containing steel weld metals. *ISIJ International* 55(8): 1730–1738. DOI: 10.2355/isijinternational.ISIJINT-2014-800

50. Kang, Y., Jeong, S., Kang, J.-H., and Lee, C. 2016. Factors affecting the inclusion potency for acicular ferrite nucleation in high-strength steel welds. *Metallurgical and Materials Transactions A* 47: 2842–2854. DOI: 10.1007/s11661-016-3456-0

51. Ramprasad, T., Mane, P., and Zega, T. J. 2018. Transmission electron microscope analysis of a spinel-perovskite assemblage within a refeactory inclusion from the northwest Africa (nwa) 5028 CR_2 chondrite. *49th Lunar and Planetary Science Conference.*

TAO DAI, **ZHILI FENG** (*fengz@ornl.gov*), **DOUGLAS KYLE**, and **S. A. DAVID** are with the Materials Science and Technology Division, Oak Ridge National Laboratory, Oak Ridge,Tenn. **KATHERINE M. SEBECK**, **DEMETRIOS A. TZELEPIS**, **KATHERINE VIEAU**, and **MATTHEW ROGERS** are with the U.S. Army DEVCOM GVSC, Warren, Mich.